

Collisionless shock heating of heavy ions in SN 1987A

Marco Miceli^{*,1,2}, Salvatore Orlando², David N. Burrows³, Kari A. Frank⁴, Costanza Argiroffi^{1,2},
Fabio Reale^{1,2}, Giovanni Peres^{1,2}, Oleh Petruk⁵, Fabrizio Bocchino²

¹*Dipartimento di Fisica e Chimica, Università di Palermo, Piazza del Parlamento 1, 90134
Palermo, Italy*

²*INAF-Osservatorio Astronomico di Palermo, Piazza del Parlamento 1, 90134 Palermo, Italy,*

³*Department of Astronomy and Astrophysics, Pennsylvania State University, University Park, PA
16802, USA*

⁴*Northwestern University, Technological Institute, 2145 Sheridan Road, Evanston, IL 60208-3112,
USA*

⁵*Institute for Applied Problems in Mechanics and Mathematics, Naukova Str. 3-b, UA-79060 Lviv,
Ukraine*

**1 Astrophysical shocks at all scales, from those in the heliosphere up to the cosmological shock
2 waves, are typically “collisionless”, because the thickness of their jump region is much shorter
3 than the collisional mean free path. Across these jumps, electrons, protons, and ions are ex-
4 pected to be heated at different temperatures. Supernova remnants (SNRs) are ideal targets
5 to study collisionless processes because of their bright post-shock emission and fast shocks.
6 Although optical observations of Balmer-dominated shocks in young SNRs showed that the
7 post-shock proton temperature is higher than the electron temperature, the actual depen-
8 dence of the post-shock temperature on the particle mass is still widely debated¹. We tackle
9 this longstanding issue through the analysis of deep multi-epoch and high-resolution obser-**

vations of the youngest nearby supernova remnant, SN 1987A, made with the *Chandra* X-ray
 telescope. We introduce a novel data analysis method by studying the observed spectra in
 close comparison with a dedicated full 3-D hydrodynamic simulation. The simulation is able
 to reproduce self-consistently the whole broadening of the spectral lines of many ions alto-
 gether. We can therefore measure the post shock temperature of protons and selected ions
 through comparison of the model with observations. We have obtained information about
 the heating processes in collisionless shocks by finding that the ion to proton temperature
 ratio is always significantly higher than one and increases linearly with the ion mass for a
 wide range of masses and shock parameters.

Shock waves are abrupt transitions between a supersonic and a subsonic flow which trans-
 form bulk kinetic energy into thermal energy by compressing and heating the medium. In the
 Earth's atmosphere the width of a shock front is of the order of a few molecular mean free paths.
 In the rarefied astrophysical environments, however, particle–particle interactions (Coulomb col-
 lisions) are typically not sufficient to provide the viscous dissipation, and collective effects, such as
 electromagnetic fluctuations and plasma waves, provide the Rankine-Hugoniot² jump conditions
 at the shock front^{3,4}. These conditions derive from the mass, momentum, and energy conservation
 across the shock and predict that the post-shock temperature T depends on the shock velocity v_s as
 $kT = 3/16 mv_s^2$, where m is the particle mass. In a plasma with different particle species, it is still
 not clear whether a (partial) temperature equilibration between different species can be reached, or
 particles with different masses reach temperatures proportional to their mass as

$$kT_i = \frac{3}{16}m_i v_s^2 \quad (1)$$

where m_i is the particle mass for the i -th species. Collisionless shocks have been observed decades

ago in the solar wind⁵, as well as on cosmological scales³. A post-shock temperature proportional to the particle mass is expected in case of scattering isotropization of the incoming particles by plasma waves. Nevertheless, partial equilibrium between different species is also possible and the validity of equation (1) is far from being settled. Thus, the actual conditions of the post-shock plasma are still under debate.

Pioneering works have shown the importance of Balmer-dominated shock fronts in SNRs as diagnostic tools^{6,7} and the study of the $H\alpha$ line profile is widely used to measure the electron to proton temperature ratio T_e/T_p ^{1,8}. However, this ratio is typically much higher than the electron to proton mass ratio (m_e/m_p) and can increase up to 1 in slow ($v_s \sim 400 \text{ km s}^{-1}$) shocks^{9,10}, showing a dependence on the shock velocity which has been modelled as $T_e/T_p \propto v_s^{-2}$. This can be explained if the immediate electron post-shock temperature does not depend on the shock velocity¹¹ (and is always $kT_e \sim 0.3 \text{ keV}$), while T_p varies as in equation (1). This behaviour can be associated with a mechanism of electron heating due to lower hybrid waves in the shock precursor¹², though other scenarios have been proposed¹³. The general expectation is that there can be different plasma instabilities that can enhance T_e/T_p above the expected value m_e/m_p and the electron heating processes in collisionless shocks are different from those of ions^{3,14,15}. Therefore, it is necessary to accurately measure the ion temperatures to test equation (1).

However, the measurement of the post shock temperatures for different ions has produced **different** results⁸: the temperature of oxygen ions relative to protons was found to be less than that predicted by equation (1) in the analysis of UV observations of SN 1006¹⁶, while it was found to be higher than equation (1) predictions in interplanetary shocks¹⁷. Recently, an important result

has been obtained in SN 1006, with He, C and N ion temperatures being consistent with the mass-proportional scenario¹⁸. Stronger constraints need to be obtained by testing equation (1) over a wider range of masses, by inspecting elements heavier than N, or O. To this end, the X-ray band is the ideal window in which bright emission lines of heavy ions are typically observed. Up to now, only in one case X-ray spectra were used to measure a line broadening of the OVII line triplet, corresponding to an extremely high oxygen temperature (~ 300 keV) in an isolated ejecta knot of SN 1006^{19,20}.

SN 1987A in the Large Magellanic Cloud offers a unique opportunity of observing a nearby, young, bright, SNR with high level of detail. SN 1987A was a hydrogen-rich core-collapse SN discovered on 1987 February 23²¹. Its evolution has been extensively covered by a wealth of observations in different wavelengths^{22–24} and reveals a complex interaction of the blast wave with the surrounding inhomogeneous medium, characterized by a dense, clumpy ring-like nebula, inside a more diffuse HII region. The interaction with the nebula is best revealed in X-rays and SN 1987A has been monitored through dedicated campaigns of observations with *XMM-Newton* and *Chandra*.

The series of X-ray observations encodes information about the physical properties of both the nebula and the stellar ejecta and requires a thorough data analysis: phenomenological models only analyzed single observations, regardless of the whole succession of data sets. Here, in our novel approach, a single 3-D hydrodynamic model²⁵ describes the evolution of SN 1987A from the onset of the supernova to the current age and accounts self-consistently for all the observations and for the evolution of the system. The reliability of the model has been tested and confirmed

by synthesizing light curves, images, and low-resolution (CCD) spectra from the hydrodynamic simulations. We found that our model self-consistently fits: i) the bolometric light curve during the first 250 days of evolution, ii) the soft (0.5 – 2 keV) and hard (3 – 10 keV) X-ray light curves in the subsequent 30 years, iii) the evolution of the morphology of the X-ray emission, iv) *XMM-Newton* EPIC and *Chandra* ACIS spectra at different epochs²⁵. Here we use this forward modeling approach to obtain deeper insight into the physics of shock heating, through the detailed reproduction of the multi-epoch high-resolution gratings X-ray observations of SN 1987A.

To synthesize the *Chandra* gratings spectra from the model, we included all the sources of line broadening, namely: i) the bulk velocities of the different parts of the ring, ii) the instrumental broadening (due to both line response function and X-ray source extension in the dispersion direction), and iii) the thermal broadening. To add the contribution of thermal heating in our synthetic spectra, we assumed the ion temperature to be mass-proportional with respect to the proton temperature. The latter is accurately followed by our hydrodynamic code, which includes a detailed model of shock heating¹¹ and post-shock evolution due to Coulomb collisions between protons and electrons²⁶ (see Sect. M1 and Sect. M2 for further details). We produced synthetic spectra either with or without thermal broadening. By comparing the synthetic line widths with those measured in the actual spectra, we were able to infer the role of thermal broadening and its dependence on the ion mass.

We considered the two deepest observations of SN 1987A performed with the MEG spectrometer of the *Chandra* High Energy Transmission Grating (HETG). The two data sets mark two different evolutionary states and different conditions in the shocked plasma: the first one consists

of a set of 14 exposures performed between March and April 2007 (SN days 7321–7358, total exposure time of 354.9 ks) and corresponds to the initial phase of interaction between the blast-wave and the circumstellar ring, while in the second one (4 HETG exposures, March 2011, 178 ks) the shock has already crossed the bulk of the ring and the X-ray flux is ~ 2 times higher than in 2007²⁷.

The hydrodynamic model simulates the evolution of the ring throughout this time range. Upper panels of Fig. 1 show the observed and synthetic X-ray images of SN 1987A in 2007 and 2011, while central panels show the comparison between the observed high resolution spectra and the synthetic spectra derived from our hydrodynamic simulations including all the possible sources of line broadening. The model agrees closely with the observations and matches in detail the X-ray spectra in both epochs (**reduced $\chi^2 = 1.95, 1.21$ with 2109 d.o.f. in 2007, 2011, respectively**), where emission lines from Fe XVII and He-like and H-like ions of Ne, Mg, and Si are visible.

The model reproduces even the significant line broadening of the single lines (lower panels of Fig. 1), which results from a combination of Doppler effects, due to the bulk velocities of the approaching and receding parts of the ring, thermal broadening, associated with the high temperatures of ions, and instrumental effects. Previous works neglected thermal broadening and used the line widths to derive *a posteriori* the bulk velocity of the plasma^{28–30}. Our model provides us with complete information to derive the total line broadening and its evolution in a self-consistent way, i. e., all the hydrodynamics and thermodynamics, and the bulk motion of the shocked plasma at all times. In particular, the Doppler broadening depends on the ring and clump densities (which affect the post-shock dragging) and on the density/velocity profiles of the outer ejecta; all these param-

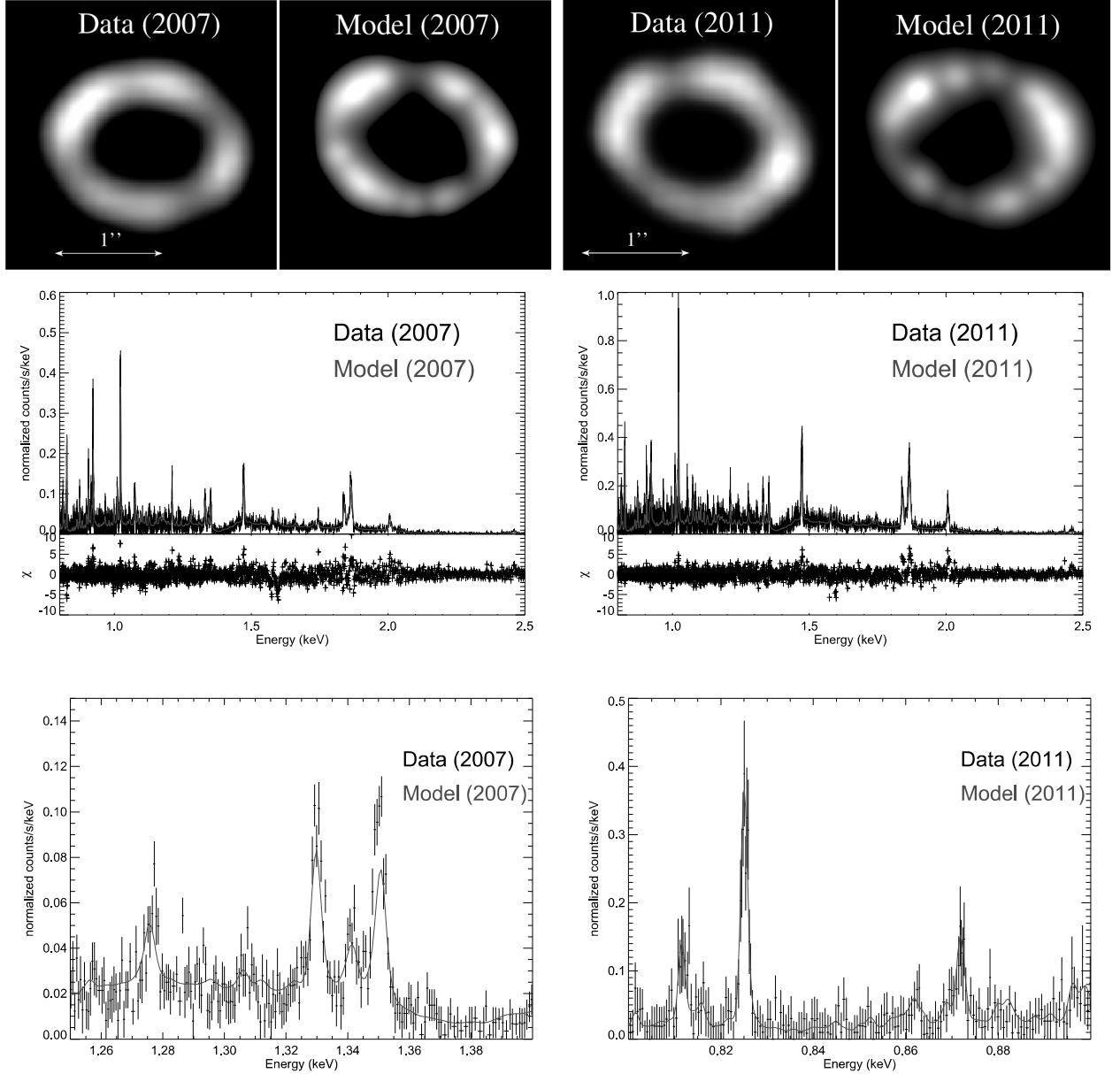


Figure 1: *Upper panels:* Observed and synthetic maps of SN 1987A in the 0.5 – 2 keV band in 2007 (left) and 2011 (right). *Central panels:* Observed (black) and synthetic (red, with all sources of line broadening) spectra in the 0.8 – 2.5 keV band (MEG +1 order of the *Chandra* HETG) in 2007 (left) and 2011 (right) with the corresponding residuals. *Lower panels:* close-up views of the central panels in the 1.25 – 1.4 keV band (in 2007, left) and 0.8 – 0.9 keV band (in 2011, right).

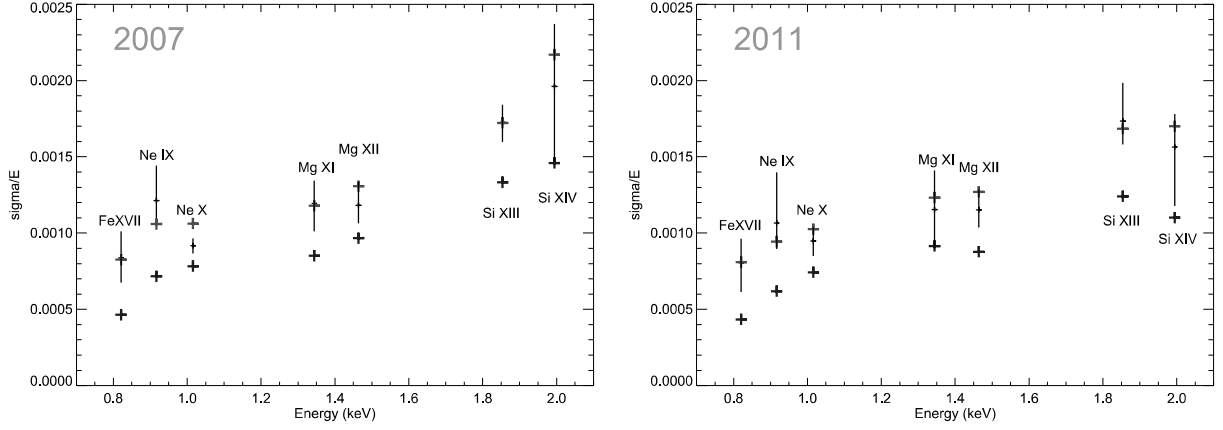


Figure 2: Line broadening for selected ions in the 2007 (*left panel*) and 2011 (*right panel*) X-ray spectra of SN 1987A: black crosses show the observed values (MEG +1 order of the *Chandra* HETG), line broadenings synthesized from our model by considering both Doppler and instrumental broadening are indicated by the blue crosses, while synthetic line broadenings with Doppler, instrumental and thermal broadening are indicated by the red crosses. Error bars are at the 90% confidence level.

ters are very well constrained by our model. To highlight the contribution of thermal broadening, we compare in Fig. 2 the line broadening derived from the model (either with or without thermal contribution) with the observed line widths for the two data sets. The figure clearly shows that the line broadening from the model without thermal contribution is large and changes from line to line and in time, as the shock expands through different parts of the ring. Nevertheless, it is always significantly smaller than the observed one, i.e., the bulk motion of the gas is not sufficient to explain the observed line broadening.

The line widths derived from the model by including also the thermal broadening are indicated by the red crosses in Fig. 2 and are in excellent agreement with those observed, for all the

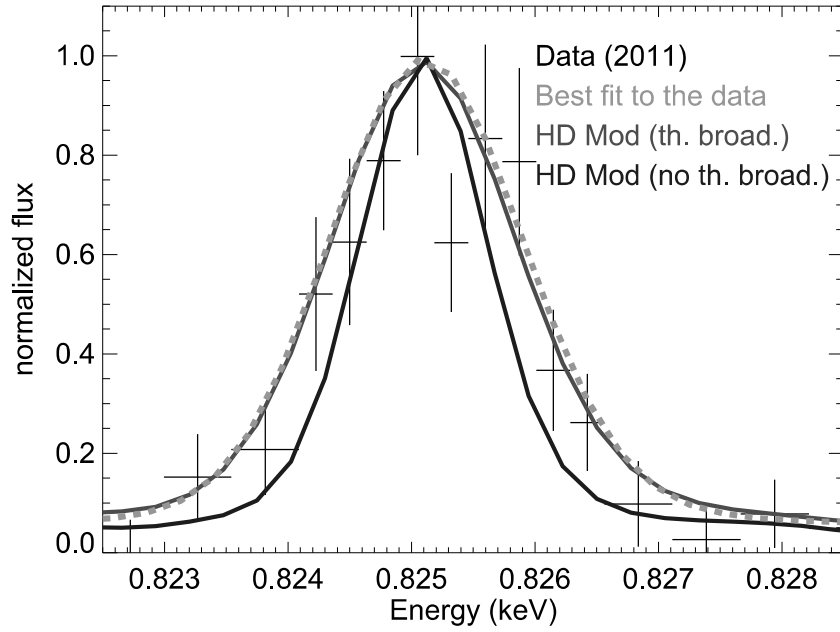


Figure 3: Fe XVII line profile derived by our hydrodynamic model for 2011 with (red curve) and without (blue curve) thermal broadening, together with the corresponding 2011 *Chandra* data (black crosses) and the Gaussian best fit to the data (green dashed curve).

ions, and for the 2007 and 2011 observations (see also Fig. 3).

To quantitatively check whether equation (1) holds for the different ions, we derived the post-shock ion temperatures $T_i(Ne, Mg, Si, Fe)$ through the difference between the observed line widths and **those predicted by the model considering only Doppler and spatial effects** (black and blue crosses in Fig. 2). The corresponding proton temperatures can be derived from our model. We found that the ion to proton temperature ratio increases monotonically with the ion mass both for the 2007 and the 2011 data sets. Given that the two observations provide consistent results, we combined them, by also combining the results from different ionization states of the same elements to further reduce the error bars.

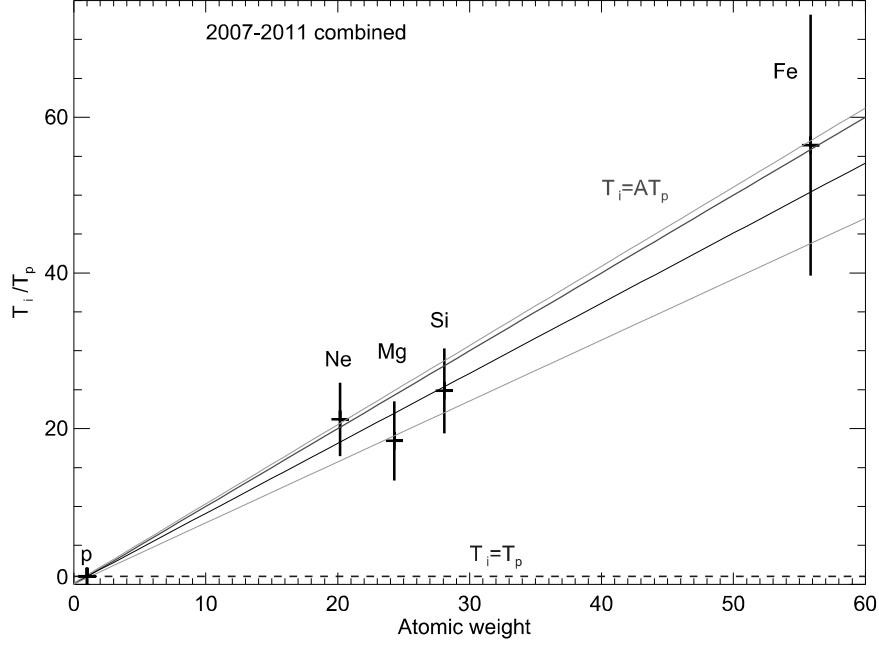


Figure 4: Ion to proton temperature ratios measured by combining the 2007 and 2011 observations of SN 1987A for Ne, Mg, Si, and Fe lines (with corresponding 90% error bars). The red line marks the mass-proportional trend predicted by equation (1), while the black line shows the best fit trend, with the corresponding 90% confidence range indicated by green lines.

Figure 4 shows the post-shock Ne, Mg, Si, and Fe temperatures normalized to the corresponding proton temperatures. We performed a simple linear regression on the data points in the figure, finding that the ion to proton temperature ratio T_i/T_p increases with the ion mass A as $T_i/T_p = kA$ with $k = 0.90 \pm 0.12$. Therefore, the ion post-shock temperature is consistent with being mass-proportional. This result is in agreement with predictions of hybrid simulations of collisionless shocks³¹.

In summary, through the combination of high-resolution X-ray spectra and 3-D hydrodynamic modeling, we ascertained the physical origin of the observed line profiles in SN 1987A, by

141 pinpointing the roles of Doppler and thermal broadening. Our results unequivocally show that post-
142 shock temperatures increase linearly with particle mass over a wide range of masses, previously
143 unexplored. This is a validation of equation (1) for ions and probes the ion heating mechanism of
144 collisionless shocks. By analyzing multi-epoch observations performed at different phases of the
145 shock-ring interaction, we also showed that the mass-proportional heating mechanism holds for
146 different shock parameters.

METHODS

M1 Proton and electron temperatures in the hydrodynamic model

The model adopted here relies on the combination of a 1-D Lagrangian code of the SN explosion, which is able to simulate the bolometric lightcurve and time evolution of the photospheric velocity and temperature of SN 1987A during the first 250 days of evolution, and a full 3-D HD code, which reproduces the expansion of the remnant between days 1 and 15,000 after the SN²⁵. The model setup, equations, and implementation, as well as its capability of reproducing observables, have been already confirmed and discussed²⁵. We here focus on the treatment of the temperature evolution in the shocked plasma. The proton temperature in the immediate post-shock region is calculated through the canonical equation $kT_p = 3/16 m_p v_s^2$. Electrons are heated at the shock front up to $kT \sim 0.3$ keV (regardless of the shock Mach number), as suggested¹¹ for shock velocities of the order of 10^3 km s⁻¹, like those in our simulations. We then calculate the evolution of proton and electron temperatures in each computational cell of the post-shock medium by considering the effects of the Coulomb collisions in the time $\Delta t = t - t_s$ where t is the current time and t_s is the time when the plasma in each computational cell was shocked (this is important also to account for the non equilibrium of ionization effects, see next Section). The electron to proton temperature ratio T_e/T_p therefore depends on the shock velocity and on the time elapsed after the shock impact.

Figure 5 shows the distribution of the emission measure of the X-ray emitting plasma in

166 the computational cells¹ vs. T_e/T_p at $t = 20$ yr and $t = 24$ yr (after the supernova explosion,
 167 corresponding to year 2007 and 2011, respectively). The figure clearly reveals the contribution of
 168 the dense clumps in the ring, (where the shock velocity is relatively low and $T_e/T_p \sim 1$), of the
 169 interclump medium within the ring ($T_e/T_p \sim 0.2 - 0.6$), and of the hotter and relatively tenuous
 170 HII region (high shock velocity and $T_e/T_p \sim 0.01 - 0.3$).

171 It is worth noting that Coulomb collisions can produce significant variations of T_e from the
 172 immediate post-shock value on a short timescale. On the other hand, the evolution of the proton
 173 temperature is much slower and T_p varies always less than 10% with respect to the immediate
 174 post-shock values over the time spanned by our simulation. Therefore T_p , as well as T_i reflects
 175 closely the immediate post-shock conditions in SN 1987A. Over the computational domain, T_e
 176 ranges between $\sim 3.5 \times 10^6$ K and $\sim 5 \times 10^7$ K, while T_p is in the range $3.5 \times 10^6 - 8 \times 10^8$ K.

177 **Coulomb collisions between different ion species and between ions and protons are not**
 178 **included in our model. From the parameters of our simulations it is possible to estimate**
 179 **the thermal equilibration time-scale for ion and protons²⁶. As for the ion-ion interactions,**
 180 **the e-folding time for the temperature evolution is of the order of a century, which is much**
 181 **higher than the time elapsed after the shock impact (the shock reached the ring in 2001 and**
 182 **we are looking at the 2007 and 2011 data), so this process is indeed negligible. As for the**
 183 **ion-proton interactions, instead, the e-folding time is comparable to the time elapsed after**
 184 **the shock impact. However, for the very turbulent magnetic field that we expect in the post-**
 185 **shock region³², the thermalization time-scale increases³³ by a factor ~ 5 , thus making this**

¹All the cells have the same volume.

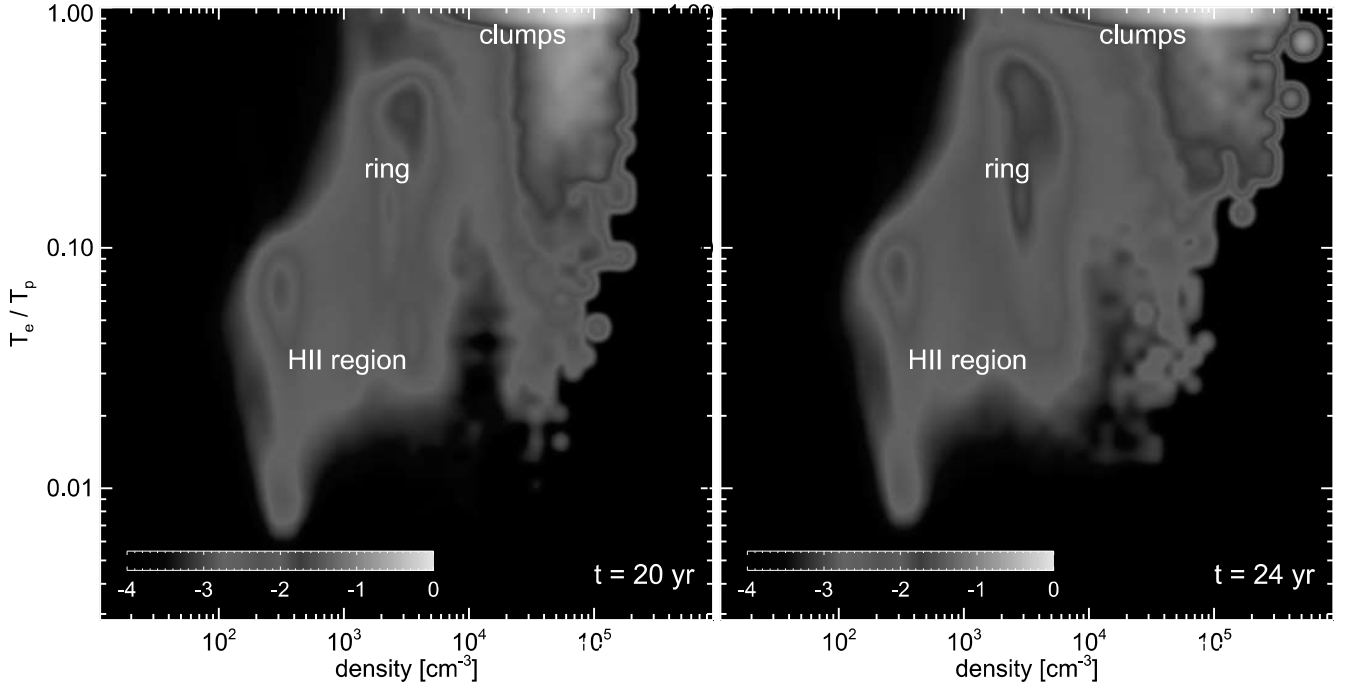


Figure 5: Distribution of emission measure vs. T_e/T_p and plasma density over the computational domain obtained from our hydrodynamic model at $t = 20$ yr and $t = 24$ yr. In each panel the color scale is logarithmic and normalized to the maximum.

process negligible for our case.

The electron to proton temperature ratio has been measured at the reverse shock of SN 1987A through the analysis of HST-COS observations³⁴ performed in 2011 (i. e., at $t = 24$ yr), showing that $T_e/T_p \approx 0.14 - 0.35$ (this value can slightly change with different assumptions, but $T_e/T_p > 0.1$ is always required to explain the data³⁴). We calculated T_e/T_p at the reverse shock from our hydrodynamic model at $t = 24$ yr (correspond to 2011). To this end, we considered only the computational cells consisting of hot ($kT \geq 0.3$ keV) ejecta material by more than 99 per cent². This selection allows us to isolate the shocked (i. e., high temperature) ejecta in the immediate post-shock region (in the post-shock flow, the ejecta are rapidly mixed with the shocked circumstellar

²The ejecta material can be identified thanks to a passive tracer included in the calculation²⁵

medium and the percentage of ejecta in the computational cells rapidly drops below 99 per cent), thus selecting a narrow sheet of plasma behind the reverse shock. We then computed the density-weighted average value of the electron to proton temperature ratio for these cells, finding $T_e/T_p = 0.155$, in remarkable agreement with that inferred from the observations. This provides a further indication of the reliability of our model.

M2 Synthesis of X-ray spectra

From the model results, we synthesized the *Chandra* HETG X-ray spectra from the values of T_e , density, and ionization time scale (computed on the basis of the plasma density and time elapsed after the shock heating) by adopting the ATOMDB V3.0.8 database. **We adopted the VNEI model within XSPEC which requires, as input, the electron temperature and the plasma ionization time scale to compute the continuum and line emission** and followed the same approach as in previous studies^{25,35,36}. The X-ray spectrum from each cell was filtered through the photoelectric absorption by the ISM, with the appropriate column density³⁷. All the synthetic spectra are folded through the *Chandra* instrumental response. In addition, to synthesize the line profiles of the *Chandra* HETG spectra, we also accounted for the three possible sources of line broadening, namely i) the angular extension and morphology of the source, i. e., the position of each X-ray emitting cell in the computational domain³, ii) the Doppler broadening, associated with the bulk velocity of the plasma, and iii) the thermal broadening, due to the ion temperature, as explained in detail below.

³The shape of the emission lines reflects the shape of the zero order spatial structure convolved with the instrumental line spread function

SN 1987A is resolved by the mirrors of *Chandra* that clearly show a ring-like morphology for the X-ray-emitting plasma which is very similar to that predicted by our model (see Fig. 1). The morphology of the X-ray emission results from a shocked circular equatorial ring whose symmetry axis is tilted with respect to the line of sight. In our simulation, we assumed the SN explosion at the origin of a 3D Cartesian coordinate system, and the dense equatorial ring on the (x, y) plane. We then rotated the system about the three axes to fit the actual inclination of the ring as found from the analysis of optical data³⁸, namely $\theta_x = 41^\circ$, $\theta_y = 8^\circ$, and $\theta_z = 9^\circ$. The projected (in the plane of the sky and in the direction of dispersion) angular distance of each X-ray emitting plasma element from the center of the ring in the zero order image determines a wavelength offset corresponding to $\Delta\lambda = 0.01112 \text{ \AA}$ per pixel, where the pixel size is $0.492''$, in the *Chandra* MEG spectra. We therefore included this effect in synthesizing the spectra from the model for each computational cell, by taking into account the actual roll angle of the *Chandra* observations, where the ± 1 arms of the dispersion axis are aligned approximately south/north, respectively. We note that the synthetic zero order images are $\sim 10\%$ smaller than those observed (Fig. 1) and we verified that this is not an issue for the spectra in the MEG +1 diffraction order described here. In fact, if we artificially enhance the angular size of the synthetic maps by a $\sim 20\%$ (i. e. making them larger than those observed) and compute the line broadening accordingly, the width of the lines increases only by $< 1\%$ for the +1 order, thus not affecting our results and conclusions. While MEG -1 order spectra are more sensitive to this issue, the +1 order spectra discussed here do not change significantly. This is because in the +1 order the effects of the angular extension of the source are somehow counterbalanced by Doppler effects, as explained below.

We computed the effects of the Doppler broadening associated with the bulk motion of the

post-shock plasma in the computational cells by taking into account the inclination of the ring
 with respect to the line of sight. **Figure 6 shows a cut of the plasma velocity along the line
 of sight, for the X-ray emitting plasma, in the plane identified by the line of sight and the
 North direction in the sky, at $t = 20$ yr and $t = 24$ yr. The two parts of the ring intercepted
 by the plane of the cut are visible as indentations with low velocity, in the upper left and
 lower right parts of the plot. Since the X-ray emission scales as the square of the particle
 density, we also plot the corresponding cuts of density to show the different weight (for the
 emerging spectrum) of the plasma velocities in different regions of the model.** We verified
 that by changing the value of θ_x by $\pm 5^\circ$ (i. e., more than the observational uncertainty on this
 parameter³⁸) the width of the synthetic lines changes only by $< 0.5\%$ in the $+1$ order, thus leaving
 all our conclusions unaffected. Because of the inclination of the ring with respect to the line of
 sight, as the shock expands, the X-ray emission of the plasma in the northern part of the ring
 will be, on average, blue-shifted, while that originating in the southern part of the ring will be
 red-shifted. Since in the $+1$ order the dispersion axis is pointing to south, the effects of Doppler
 broadening and that of the angular extension of the source work in opposite directions, while they
 sum up in the -1 order (whose dispersion axis points to north). Therefore, the combined effects of
 the source angular extension and of Doppler broadening make the emission lines broader in the -1
 order with respect to the $+1$ order, as already pointed out by several works^{28,29,39} for the analysis
 of the actual *Chandra* spectra. Because of this, the relative contribution of thermal broadening
 (which is, in absolute, the same in the $+/-1$ orders) to the total line broadening, will be higher in
 the $+1$ spectra.

As explained in Sect. M1 we followed the evolution of T_p and T_e in the post-shock flow.

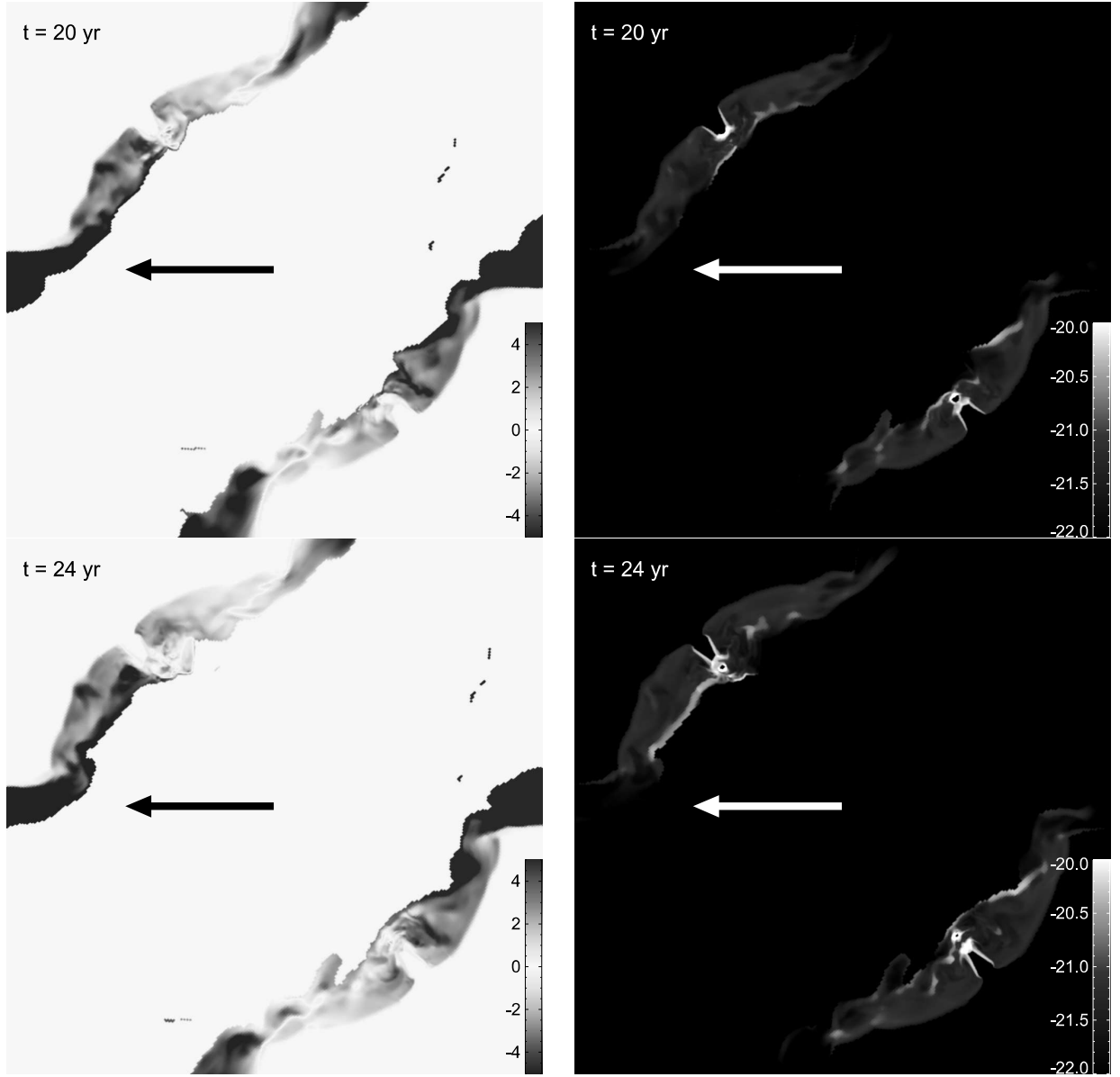


Figure 6: *Upper panels:* Cut of the plasma velocity along the line of sight, for the X-ray emitting plasma, in the plane identified by the line of sight and the North direction in the sky at $t = 20$ yr (*left*), with the corresponding cut of plasma density (*right*). The velocity is in units of 10^3 km s^{-1} , the density in g cm^{-3} . The arrow points to the observer. *Lower panels:* same as upper panels for $t = 24$ yr

Electron temperature, together with ionization time scale, plasma density and bulk velocity, allow us to synthesize the emerging X-ray spectrum from each computational cell, while the local value of T_p allows us to derive the thermal line broadening, as explained below. To include the effects of thermal broadening, we considered the values of T_p in each cell and assumed that ions with atomic weight A have temperature $T_i^{mod} = AT_p$, as in equation (1). On the basis of our assumption, we can add in quadrature a Gaussian broadening with

$$\sigma_{th} = E \sqrt{\frac{kT_i^{mod}}{m_i c^2}} = E \sqrt{\frac{kT_p}{m_p c^2}} \quad (2)$$

where E is the energy of the emission line, k is the Boltzmann constant, and c the speed of light. In this way, from T_p we can synthesize from our simulations the line broadening expected in case of mass-proportional post-shock temperature. We then compare the synthetic line broadening with that observed to test the mass-proportional assumption against actual observations, as explained in Sect. M4.

We fitted the synthetic line profiles with Gaussians to measure their widths. The widths for selected emission lines in the +1 order spectra obtained either with (red crosses) or without (blue crosses) thermal broadening at $t = 20$ yr and $t = 24$ yr are shown in Fig. 2, while Fig. 7 shows the widths for the -1 order at $t = 24$ yr. As expected, the total line broadening is higher in the -1 order and this makes the estimate of ion and proton temperatures difficult when comparing models and observations (see Sect. M4).

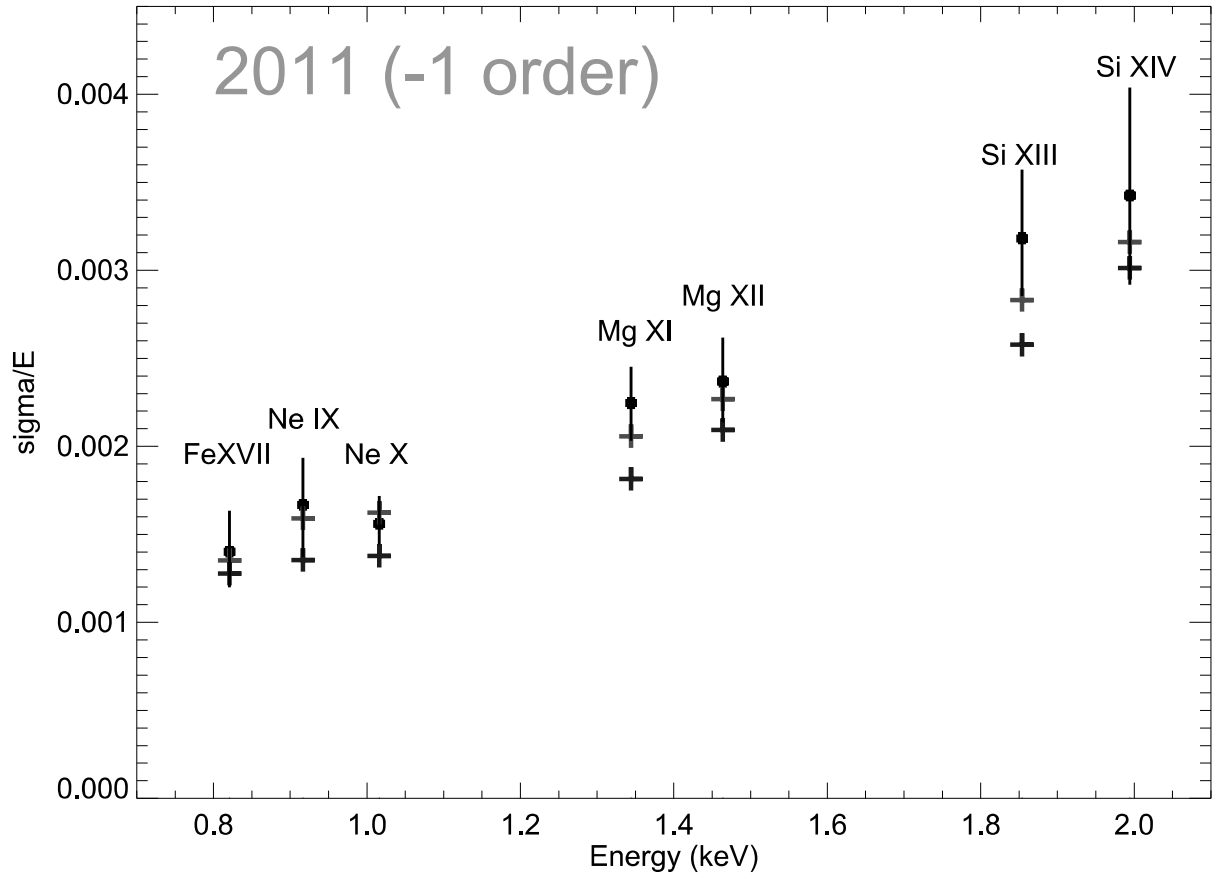


Figure 7: Line broadening for selected ions in the 2011 X-ray spectra of SN 1987A: black crosses show the observed values (MEG -1 order of the *Chandra* HETG), while red and blue crosses indicate the values synthesized from our hydrodynamic model with and without including the effects of thermal broadening, respectively. Error bars are at the 90% confidence level.

M3 Data Analysis

We analyzed *Chandra* observations 7588 – 90, 8487, 8488, 8523, 8537 – 9, 8542 – 6 (PI C. Canizares) performed between March and April 2007 with a total exposure time of 354.9 ks and observations 12145, 12146, 13238, 13239 (PI C. Canizares) performed on March 2011 for a to-

tal exposure time of 178 ks. All observations have pointing coordinates $\alpha_{J2000} = 5^h 35^m 28.0^s$,
 $\delta_{J2000} = -69^\circ 16' 11.0''$ and were reprocessed with CIAO 4.9 and CALDB 4.7.3.

We extracted the MEG $+/-1$ spectra by producing the corresponding arf (with the *fullgarf* script) and rmf (with the *mkgrmf* script) files. We then combined all the 14 spectra of the same order for the 2007 exposures and the 4 spectra of the same order for the 2011 exposures by adopting the *combine_grating_spectra*, thus obtaining cumulative $+1$ order and -1 order MEG spectra for the two epochs.

Spectral analysis has been performed with XSPEC V12.9.1. We fitted the single lines in narrow bands by adopting Gaussian components plus a thermal bremsstrahlung component (to fit the continuum). We also included the interstellar absorption (TBABS model within XSPEC) in all the spectral fittings, by fixing the absorbing column density to $N_H = 2.35 \times 10^{21} \text{ cm}^{-2}$, in agreement with previous results of the analysis of Chandra data³⁷. As explained in Sect. M2 we measure higher line widths in the -1 order than in the $+1$ order. The best-fit parameters are shown in Table 2.

M4 Diagnostics from the comparison between models and observations

The procedure adopted to compare models and data is summarized in the flow chart shown in Fig. 9 and described below. First, from our hydrodynamic simulations, we synthesize X-ray spectra without including the effects of thermal broadening and compare them against the actual *Chandra* data. We find that these synthetic spectra severely underestimate the observed line broadening (both in 2007 and 2011), as shown in Fig. 2. This proves that

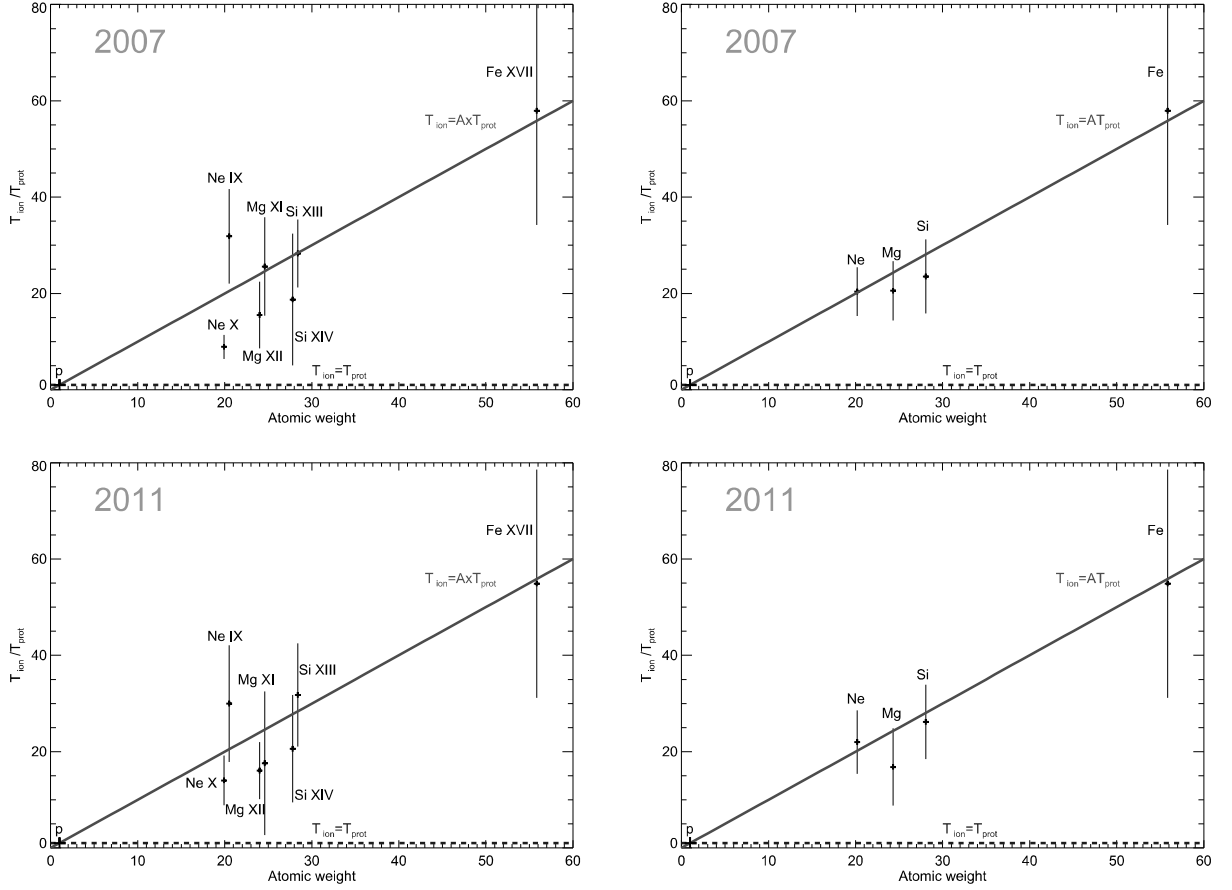


Figure 8: *Upper panels:* Ion to proton temperature ratios measured for the 2007 observations of SN 1987A for selected emission lines (*left*) and by averaging the values over different ionization stages of the same element (*right*) with the corresponding 90% error bars. The red line marks the mass-proportional trend predicted by equation (1). *Lower panels:* same as upper panels for the 2011 observations.

Doppler broadening and spatial extension of the source cannot reproduce the total observed line widths, and an additional source of broadening, associated with high ion temperatures, is necessary to explain the data. We therefore measure the ion temperatures, T_i , in SN 1987A from the difference⁴ between the observed line widths and those predicted by the model

⁴All the line width contributions are summed/subtracted in quadrature.

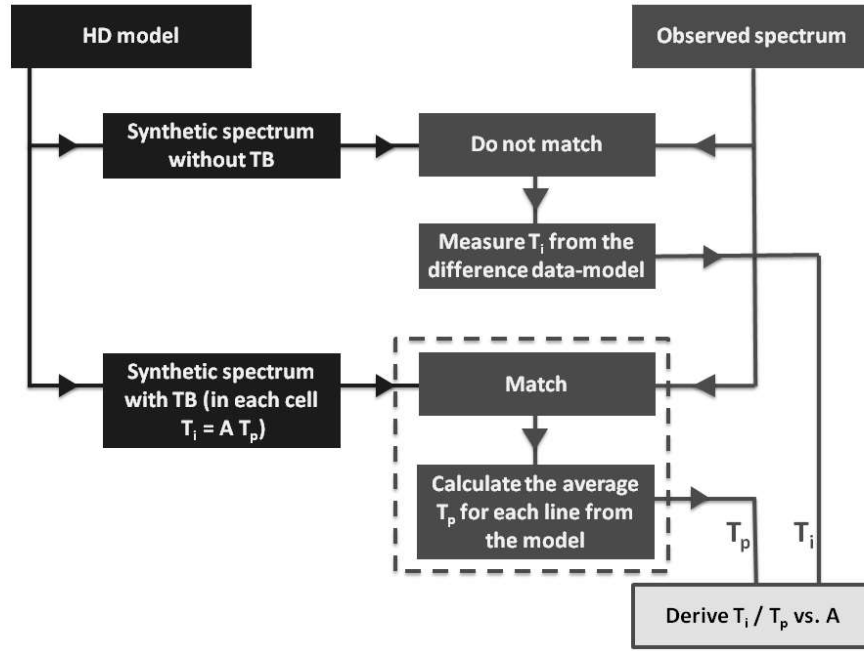


Figure 9: Flow-chart of the procedure adopted to compare models and data. Blue boxes indicate modeling, red boxes data analysis, and the information deduced from the comparison between data and model are coded in green. The dashed box marks the results and the yellow box indicates the plot presented in Fig. 4. See Sect. M4 for details.

considering Doppler and spatial effects only.

Then we checked if the model reproduces the observed line widths by including the effects of thermal broadening in the synthesis of emission. In doing this, we considered the values of T_p in each cell and assumed a mass proportional ion temperature, i. e. that ions with atomic weight A have temperature $T_i^{mod} = AT_p$, as explained in Sect. M2. Figure 2 shows that the widths of the emission lines measured in the *Chandra* spectra (both for the 2007 and 2011 observations) are in excellent agreement with the predictions. It is worth noting that,

310 **by assuming $T_i^{mod} = T_p$ the model fails in reproducing the observed line widths.** We point out
 311 that the capability of our synthetic spectra to reproduce the multi-epoch line broadening both in the
 312 $+1$ order (where the contribution of thermal broadening is higher) and in the -1 order (where the
 313 Doppler broadening dominates over thermal broadening, see Sect. M2) indicates that we correctly
 314 estimating the Doppler broadening and our results are robust.

315 **The agreement between model predictions and multi-epoch observations strongly con-**
 316 **firms the predictions of equation 1 and proves that ions are heated up to higher temperatures**
 317 **than protons, according to their mass. In particular, we point out that if actual ions were**
 318 **heated at temperature T_p (i.e., by assuming thermal equilibration between particle species at**
 319 **the shock front), the thermal width of their emission lines would not be enough to explain the**
 320 **observed broadening, being reduced by a factor ranging from ~ 4.5 (for Ne) up to ~ 7.5 (for**
 321 **Fe), as explained by equation 2.**

322 **To quantify the agreement between equation 1 and our joint modeling and data analysis**
 323 **of SN 1987A, we produced the plot shown in Fig. 4. To this end, we use the value of T_i**
 324 **deduced from the comparison between actual spectra and those synthesized from the model**
 325 **without including thermal broadening, and the corresponding proton temperature calculated**
 326 **from our hydrodynamic simulations, as explained below. It must be stressed that the global**
 327 **X-ray spectrum of SN 1987A forms from a very broad distribution of emission measure**
 328 **versus temperature (see Fig. 5) and different emission lines arise from plasma at different**
 329 **(electron and proton) temperatures. “Colder” lines (e.g., Fe XVII and Ne IX) originate where**
 330 **the plasma temperature is lower (generally, behind slow shocks like those propagating in**

the clumps), while “hotter lines” (e.g. Si XIV) stem from high temperature regions. This calls for the need to estimate the average emission-weighted proton temperature $\overline{T_p}(l)$ from the plasma contributing to each emission line (the index l runs over all the inspected lines). This is possible by comparing our synthetic spectra obtained either with or without thermal broadening. In fact, the separation between red and blue crosses in Fig. 2 depends on T_i^{mod} and provides a measure of the emission-weighted average (the average being calculated over all the domain) value of ion temperature for each line, $\overline{T_i^{mod}}(l)$, and then on $\overline{T_p}(l)$ (through equation (2)). We thus obtain the proton temperatures listed in Table 1 for each line in the +1 order spectrum. We point out that the temporal evolution of the average $\overline{T_p}$ in the different emission lines is non-trivial, depending on the expansion of the shock (i.e., contribution from newly shocked plasma), on the temporal evolution of T_e and T_p due to the Coulomb collisions, on the mixing of different plasma components, and on the complicated evolution of the distribution of emission measure (and particle density) vs. temperature and ionization time-scale.

We then divided T_i (calculated by comparing observations and synthetic spectra without thermal broadening) by the corresponding $\overline{T_p}$ (inferred from the model as explained above) and obtained the results shown in Fig. 8. It must be pointed out that, for all lines, in both epochs, T_i is always significantly higher than the proton temperature, which is extremely reliable since it depends on shock velocities and plasma densities that are very well constrained by our simulation²⁵. We then averaged the ion to proton temperature ratios for He-like and H-like ions of the same species and obtained the results shown in the right panels of Fig. 8, for 2007 (upper panel) and 2011 (lower panel). Since the two epochs provide consistent results, we further reduced the error bars by combining them, thus obtaining the

Table 1: Emission-weighted proton temperatures derived from synthetic emission lines (+1 order)
at $t = 20$ yr and $t = 24$ yr

| Emission line | $\overline{T_p}(l)$ (K) | $\overline{T_p}(l)$ (K) |
|---------------|-------------------------|-------------------------|
| | $t = 20$ yr | $t = 24$ yr |
| Fe XVII | 4.9×10^6 | 4.9×10^6 |
| Ne IX | 6.3×10^6 | 5.3×10^6 |
| Ne X | 5.4×10^6 | 5.2×10^6 |
| Mg XI | 6.9×10^6 | 7.1×10^6 |
| Mg XII | 8.1×10^6 | 8.8×10^6 |
| Si XIII | 1.2×10^7 | 1.4×10^7 |
| Si XIV | 2.6×10^7 | 1.8×10^7 |

Table 2: Best-fit parameters for the *Chandra* HETG MEG spectra

| Line | E (eV) | Width (eV) | Width (km/s) | χ^2 (d.o.f.) | E (eV) | Width (eV) | Width (km/s) | χ^2 (d.o.f.) |
|---------|------------------------|------------------------|---------------------|-------------------|--------------------------|------------------------|----------------------|-------------------|
| (2007) | (+1) | (+1) | (+1) | (-1) | (-1) | (-1) | | |
| Fe XVII | $825.1^{+0.3}_{-0.1}$ | 0.69 ± 0.14 | 250 ± 50 | 75.8 (146) | 825.1 ± 0.1 | 1.39 ± 0.09 | 500 ± 30 | 198.1 (146) |
| Ne IX | 920.9 ± 0.1 | $1.11^{+0.02}_{-0.01}$ | 362^{+7}_{-3} | 124.8 (98) | 921.2 ± 0.2 | $1.55^{+0.2}_{-0.11}$ | 500^{+70}_{-40} | 124.8 (98) |
| Ne X | 1020.82 ± 0.05 | 0.93 ± 0.05 | 273 ± 15 | 121.7 (77) | 1020.87 ± 0.10 | 1.68 ± 0.10 | 490 ± 30 | 114.0 (77) |
| Mg XI | $1350.3^{+0.1}_{-0.3}$ | 1.6 ± 0.2 | 350 ± 40 | 74.9 (100) | $1350.9^{+0.2}_{-0.3}$ | $3.2^{+0.2}_{-0.3}$ | 710^{+40}_{-70} | 165.9 (100) |
| Mg XII | $1470.6^{+0.1}_{-0.2}$ | $1.75^{+0.2}_{-0.16}$ | 360^{+40}_{-30} | 292.0 (196) | 1471.1 ± 0.3 | 3.5 ± 0.3 | 710 ± 60 | 362.1 (196) |
| Si XIII | $1862.1^{+0.2}_{-0.3}$ | 3.2 ± 0.2 | 510 ± 30 | 124.7 (67) | $1862.2^{+1.2}_{-3}$ | $5.7^{+0.8}_{-1.2}$ | 920^{+130}_{-190} | 107.5 (67) |
| Si XIV | $2004.2^{+0.6}_{-0.9}$ | $3.9^{+0.8}_{-1.0}$ | 580^{+120}_{-150} | 191.7 (112) | 2005 ± 3 | $6.5^{+2}_{-1.5}$ | 1000^{+300}_{-200} | 155.0 (112) |
| Line | E (eV) | Width (eV) | Width (km/s) | χ^2 (d.o.f.) | E (eV) | Width (eV) | Width (km/s) | χ^2 (d.o.f.) |
| (2011) | (+1) | (+1) | (+1) | (-1) | (-1) | (-1) | | |
| Fe XVII | $825.0^{+0.2}_{-0.16}$ | $0.66^{+0.13}_{-0.16}$ | 240^{+50}_{-60} | 44.3 (146) | 825.0 ± 0.2 | 1.3 ± 0.2 | 470 ± 70 | 111.2 (146) |
| Ne IX | 921.2 ± 0.2 | $0.98^{+0.13}_{-0.15}$ | 320^{+40}_{-50} | 91.6 (98) | $921.53^{+0.14}_{-0.08}$ | $1.5^{+0.3}_{-0.2}$ | 490^{+100}_{-70} | 71.0 (98) |
| Ne X | 1020.95 ± 0.09 | 0.96 ± 0.09 | 280 ± 30 | 51.9 (77) | $1021.03^{+0.2}_{-0.12}$ | $1.58^{+0.19}_{-0.10}$ | 460^{+60}_{-30} | 71.4 (77) |
| Mg XI | $1350.9^{+0.3}_{-0.2}$ | $1.6^{+0.3}_{-0.4}$ | 360^{+70}_{-90} | 102.1 (100) | $1350.9^{+0.2}_{-0.5}$ | 3.0 ± 0.3 | 670 ± 70 | 101.3 (100) |
| Mg XII | $1470.9^{+0.2}_{-0.1}$ | 1.7 ± 0.2 | 350 ± 40 | 237.3 (196) | 1471.4 ± 0.3 | $3.5^{+0.3}_{-0.4}$ | 710^{+60}_{-80} | 193.8 (196) |
| Si XIII | $1863.2^{+0.5}_{-0.9}$ | $3.2^{+0.3}_{-0.5}$ | 520^{+50}_{-80} | 94.0 (67) | $1862.1^{+0.8}_{-0.9}$ | $5.9^{+0.7}_{-0.6}$ | 950^{+110}_{-100} | 79.0 (67) |
| Si XIV | 2003.6 ± 0.5 | $3.1^{+0.5}_{-0.8}$ | 460^{+70}_{-120} | 144.9 (112) | 2006.4 ± 1.2 | $6.8^{+1.3}_{-1.0}$ | 1020^{+190}_{-150} | 96.6 (112) |

plot shown in Fig. 4 with the corresponding linear regression.

Data Availability

The HD simulations adopted here are presented in detail in Orlando et al. Supernova 1987A: a Template to Link Supernovae to Their Remnants, ApJ 810, 168 (2015). The Chandra dataset analyzed are available in the Chandra Data Archive (<http://cxc.harvard.edu/cda/>). Other relevant data are available from the corresponding author upon reasonable request.

References

- Ghavamian, P., Schwartz, S. J., Mitchell, J., Masters, A. & Laming, J. M. Electron-Ion Tem-

perature Equilibration in Collisionless Shocks: The Supernova Remnant-Solar Wind Connection. *Space Sci. Rev.* **178**, 633–663 (2013).

2. Landau, L. D. & Lifshitz, E. M. *Fluid mechanics* (Course of theoretical physics, Oxford: Pergamon Press, 1959, 1959).

3. Bykov, A. M., Dolag, K. & Durret, F. Cosmological Shock Waves. *Space Sci. Rev.* **134**, 119–140 (2008).

4. Vink, J. Supernova remnants: the X-ray perspective. *A&A Rev.* **20**, 49 (2012).

5. Tsurutani, B. T. & Stone, R. G. Collisionless shocks in the heliosphere: Reviews of current research. *Washington DC American Geophysical Union Geophysical Monograph Series* **35** (1985).

6. Chevalier, R. A. & Raymond, J. C. Optical emission from a fast shock wave - The remnants of Tycho’s supernova and SN 1006. *ApJ* **225**, L27–L30 (1978).

7. Chevalier, R. A., Kirshner, R. P. & Raymond, J. C. The optical emission from a fast shock wave with application to supernova remnants. *ApJ* **235**, 186–195 (1980).

8. Raymond, J. C. Shock Waves in Supernova Ejecta. *Space Sci. Rev.* **214**, 28 (2018).

9. Rakowski, C. E., Ghavamian, P. & Hughes, J. P. The Physics of Supernova Remnant Blast Waves. II. Electron-Ion Equilibration in DEM L71 in the Large Magellanic Cloud. *ApJ* **590**, 846–857 (2003).

10. van Adelsberg, M., Heng, K., McCray, R. & Raymond, J. C. Spatial Structure and Collisionless Electron Heating in Balmer-dominated Shocks. *ApJ* **689**, 1089–1104 (2008).

- 382 11. Ghavamian, P., Laming, J. M. & Rakowski, C. E. A Physical Relationship between Electron-
383 Proton Temperature Equilibration and Mach Number in Fast Collisionless Shocks. *ApJ* **654**,
384 L69–L72 (2007).
- 385 12. Rakowski, C. E., Laming, J. M. & Ghavamian, P. The Heating of Thermal Electrons in Fast
386 Collisionless Shocks: The Integral Role of Cosmic Rays. *ApJ* **684**, 348–357 (2008).
- 387 13. Vink, J., Broersen, S., Bykov, A. & Gabici, S. On the electron-ion temperature ratio estab-
388 lished by collisionless shocks. *A&A* **579**, A13 (2015).
- 389 14. Shimada, N. & Hoshino, M. Strong Electron Acceleration at High Mach Number Shock
390 Waves: Simulation Study of Electron Dynamics. *ApJ* **543**, L67–L71 (2000).
- 391 15. Park, J., Caprioli, D. & Spitkovsky, A. Simultaneous Acceleration of Protons and Electrons
392 at Nonrelativistic Quasiparallel Collisionless Shocks. *Physical Review Letters* **114**, 085003
393 (2015).
- 394 16. Korreck, K. E., Raymond, J. C., Zurbuchen, T. H. & Ghavamian, P. Far Ultraviolet Spectro-
395 scopic Explorer Observation of the Nonradiative Collisionless Shock in the Remnant of SN
396 1006. *ApJ* **615**, 280–285 (2004).
- 397 17. Berdichevsky, D., Geiss, J., Gloeckler, G. & Mall, U. Excess heating of $^4\text{He}^{2+}$ and O^{6+}
398 relative to H^+ downstream of interplanetary shocks. *J. Geophys. Res.* **102**, 2623–2636 (1997).
- 399 18. Raymond, J. C., Winkler, P. F., Blair, W. P. & Laming, J. M. Ion-Ion Equilibration and Particle
400 Distributions in a 3000 km s^{-1} Shock in SN 1006. *ApJ* **851**, 12 (2017).
- 401 19. Broersen, S. *et al.* The northwestern ejecta knot in SN 1006. *A&A* **552**, A9 (2013).

- 402 20. Vink, J., Laming, J. M., Gu, M. F., Rasmussen, A. & Kaastra, J. S. The Slow Temperature
403 Equilibration behind the Shock Front of SN 1006. *ApJ* **587**, L31–L34 (2003).
- 404 21. West, R. M., Lauberts, A., Schuster, H.-E. & Jorgensen, H. E. Astrometry of SN 1987A and
405 Sanduleak-69 202. *A&A* **177**, L1–L3 (1987).
- 406 22. Arnett, W. D., Bahcall, J. N., Kirshner, R. P. & Woosley, S. E. Supernova 1987A. *ARA&A*
407 **27**, 629–700 (1989).
- 408 23. McCray, R. Supernova 1987A revisited. *ARA&A* **31**, 175–216 (1993).
- 409 24. McCray, R. & Fransson, C. The Remnant of Supernova 1987A. *ARA&A* **54**, 19–52 (2016).
- 410 25. Orlando, S., Miceli, M., Pumo, M. L. & Bocchino, F. Supernova 1987A: a Template to Link
411 Supernovae to Their Remnants. *ApJ* **810**, 168 (2015).
- 412 26. Spitzer, L. *Physics of Fully Ionized Gases* (Physics of Fully Ionized Gases, New York: Inter-
413 science (2nd edition), 1962, 1962).
- 414 27. Frank, K. A. *et al.* Chandra Observes the End of an Era in SN 1987A. *ApJ* **829**, 40 (2016).
- 415 28. Zhekov, S. A., McCray, R., Borkowski, K. J., Burrows, D. N. & Park, S. Chandra Observations
416 of Shock Kinematics in Supernova Remnant 1987A. *ApJ* **628**, L127–L130 (2005).
- 417 29. Zhekov, S. A. *et al.* High-Resolution X-Ray Spectroscopy of SNR 1987A: Chandra Letg and
418 HETG Observations in 2007. *ApJ* **692**, 1190–1204 (2009).
- 419 30. Dewey, D., Dwarkadas, V. V., Haberl, F., Sturm, R. & Canizares, C. R. Evolution and Hydro-
420 dynamics of the Very Broad X-Ray Line Emission in SN 1987A. *ApJ* **752**, 103 (2012).

- 421 31. Caprioli, D., Yi, D. T. & Spitkovsky, A. Chemical Enhancements in Shock-Accelerated Parti-
422 cles: Ab initio Simulations. *Physical Review Letters* **119**, 171101 (2017).
- 423 32. Zanardo, G. *et al.* Detection of Linear Polarization in the Radio Remnant of Supernova 1987A.
424 *ApJ* **861**, L9 (2018).
- 425 33. Narayan, R. & Medvedev, M. V. Thermal Conduction in Clusters of Galaxies. *ApJ* **562**,
426 L129–L132 (2001).
- 427 34. France, K. *et al.* HST-COS Observations of Hydrogen, Helium, Carbon, and Nitrogen Emis-
428 sion from the SN 1987A Reverse Shock. *ApJ* **743**, 186 (2011).
- 429 35. Orlando, S., Drake, J. J. & Laming, J. M. Three-dimensional modeling of the asymmetric blast
430 wave from the 2006 outburst of RS Ophiuchi: Early X-ray emission. *A&A* **493**, 1049–1059
431 (2009).
- 432 36. Miceli, M., Orlando, S., Reale, F., Bocchino, F. & Peres, G. Hydrodynamic modelling of
433 ejecta shrapnel in the Vela supernova remnant. *MNRAS* **430**, 2864–2872 (2013).
- 434 37. Park, S. *et al.* Evolutionary Status of SNR 1987A at the Age of Eighteen. *ApJ* **646**, 1001–1008
435 (2006).
- 436 38. Sugerman, B. E. K., Crotts, A. P. S., Kunkel, W. E., Heathcote, S. R. & Lawrence, S. S. The
437 Three-dimensional Circumstellar Environment of SN 1987A. *ApJS* **159**, 60–99 (2005).
- 438 39. Dewey, D., Zhekov, S. A., McCray, R. & Canizares, C. R. Chandra HETG Spectra of SN
439 1987A at 20 Years. *ApJ* **676**, L131 (2008).

Acknowledgements The software used in this work was, in part, developed by the U.S. Department of Energy-supported Advanced Simulation and Computing/Alliance Center for Astrophysical Thermonuclear Flashes at the University of Chicago. We acknowledge that the results of this research have been achieved using the PRACE Research Infrastructure resource MareNostrum III based in Spain at the Barcelona Supercomputing Center (PRACE Award N.2012060993). The scientific results reported in this article are based to a significant degree on data obtained from the Chandra Data Archive. SO, MM, GP, FB acknowledge financial contribution from the agreement ASI-INAF n.2017-14-H.O.

Author Contributions M.M. composed the text on the basis of inputs from all authors. M.M. designed the analysis procedure and lead the analysis of the synthetic and actual X-ray spectra. S.O. lead the setup and run of the HD simulation and the synthesis of X-ray spectra. D.B., K.F., and C.A. supported the X-ray data analysis process. F.R., G.P., O.P., and F.B. supported the analysis of the simulation and the synthesis of observables. All authors helped to discuss the results and to comment on the manuscript.

Corresponding author Correspondence to M. Miceli (email: miceli@astropa.unipa.it).